Inorganic Chemistry

Article

pubs.acs.org/IC

Photosystem II Like Water Oxidation Mechanism in a Bioinspired Tetranuclear Manganese Complex

Rong-Zhen Liao,* Markus D. Kärkäs, Bao-Lin Lee, Björn Åkermark, and Per E. M. Siegbahn*

Department of Organic Chemistry, Arrhenius Laboratory, Stockholm University, SE-10691 Stockholm, Sweden

Supporting Information

ABSTRACT: The synthesis of Mn-based catalysts to mimic the structural and catalytic properties of the oxygen-evolving complex in photosystem II is a long-standing goal for researchers. An interesting result in this field came with the synthesis of a Mn complex that enables water oxidation driven by the mild single-electron oxidant $[Ru(bpy)_3]^{3+}$. On the basis of hybrid density functional calculations, we herein propose a water oxidation mechanism for this bioinspired Mn catalyst, where the crucial O−O bond formation proceeds from the formal $Mn_4^{IV,IV,IV,V}$ state by direct coupling of a Mn^{IV}-bound terminal oxyl radical and a di-Mn bridging oxo group, a mechanism quite similar to the presently leading suggestion for the natural system. Of importance here is that the designed ligand is shown to be redox-active and can therefore store redox equivalents during the catalytic transitions, thereby alleviating the redox processes at the Mn centers.

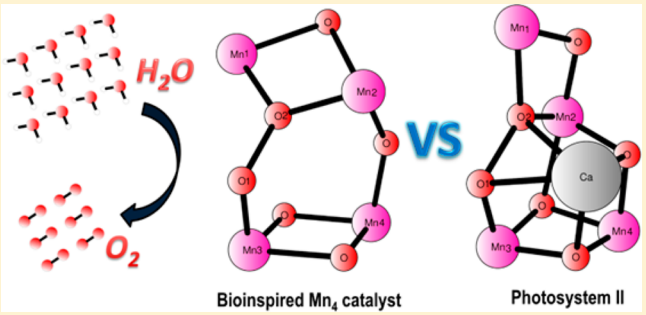

1. INTRODUCTION

Water splitting driven by light is a promising technology for supplying clean and sustainable fuel by production of hydrogen. In nature, solar energy is converted into chemical energy by abstracting electrons from water and using them to reduce carbon dioxide to biomass. In this process, water is oxidized to molecular oxygen, catalyzed by the Mn_4Ca cluster in the oxygen-evolving center (OEC) of photosystem II (PSII).[1−4] The general structure of the core of the OEC, the topology of the Mn_4Ca cluster and the ligation pattern, has been established by a high-resolution structure at 1.9 Å.[4] The oxidation of water to molecular oxygen is a four-electron process and proceeds according to the Kok cycle,[5] which cycles via five redox states, denoted S_0, S_1, S_2, S_3, and S_4. These states are produced by four sequential releases of electrons, starting with $Mn_4^{III,III,III,IV}$ and resulting in $Mn_4^{IV,IV,IV,V}$ (the S_4 state), in which O−O bond formation takes place.[6]

During the past two decades, great efforts have been devoted to the synthesis of biomimetic structural models of the OEC based on Mn.[7−16] However, only a limited number of these complexes have been shown to be capable of catalyzing evolution of oxygen, using either oxygen atom donors such as $KHSO_5$,[7,11,13] NaClO,[7] *m*-chloroperbenzoic acid,[8] and *t*BuOOH,[9,12] or, in a few cases, the single-electron oxidant Ce^{IV}.[9,10]

We have recently prepared the dinuclear $Mn_2^{II,III}$ complex **1** (Figure 1), which catalyzes water oxidation in neutral (pH 7.2) homogeneous solutions, driven by the mild single-electron oxidant $[Ru(bpy)_3]^{3+}$ (bpy = 2,2′-bipyridine).[17] Complex **1** also promotes photochemical oxidation of water utilizing a $[Ru(bpy)_3]^{2+}$-type photosensitizer and $Na_2S_2O_8$ as the electron acceptor. Attempted crystallization of the complex **1** in methanol solution resulted in the tetranuclear cluster **2** (Figure 2). Isotope labeling using $H_2{}^{18}O$ confirmed that both oxygen atoms are derived from water, suggesting that **1** is truly a water oxidation catalyst, probably after conversion to complex **3** by reaction with the phosphate buffer. Further kinetic investigations showed a turnover number (TON; defined as produced moles of O_2 per mole of catalyst) of approximately 25 and a turnover frequency (TOF; defined as produced moles of O_2 per mole of catalyst per unit time) of about 0.027 s^{-1}, which can be transferred into a barrier of about 20 kcal mol^{-1} using classical transition-state theory. The TON is far from that of the natural OEC (ca. 10^6), and the TOF of this biomimetic Mn catalyst is many orders of magnitude slower than that of the OEC, ca. 100 s^{-1}. There is thus much room for improvement of artificial Mn-based catalysts.

In recent years, quantum chemical calculations have proven to be a powerful tool in the study of both natural[18−27] and artificial[28−30] water oxidation catalysis. A wealth of chemical insight has been obtained, especially in the electronic structures of various redox intermediates and the transition states for the critical O−O bond formation. Exploratory calculations on the dinuclear form of complex **3** gave an activation energy of ca. 30 kcal mol^{-1}, which is far from the experimental value of 20 kcal mol^{-1}. However, NMR experiments suggested that complex **3** in solution was in equilibrium with a dimeric species (i.e., a tetranuclear Mn species),[17] which could perhaps be involved in the catalytic activity. It therefore seemed interesting to perform

Received: October 17, 2014
Published: December 8, 2014

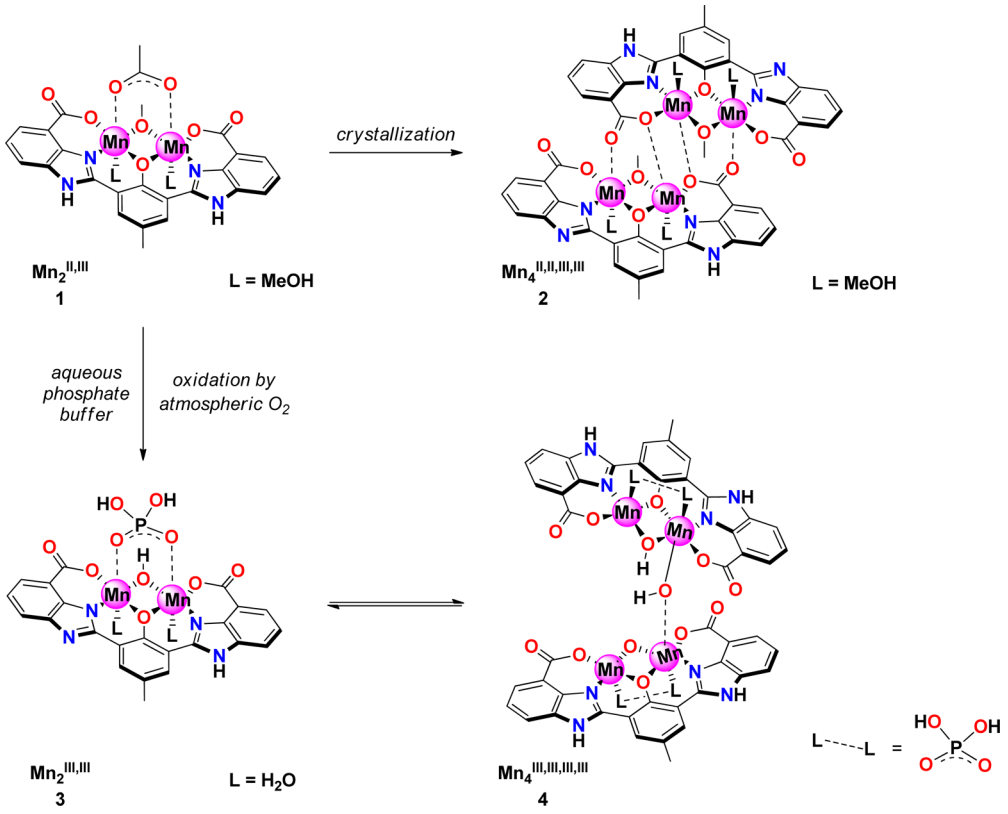

Figure 1. Schematic representations of **1** and **2** and dissolution of **2** in phosphate buffer to form **3** and **4**. For clarity, the two phosphate ligands in **4** are not shown.

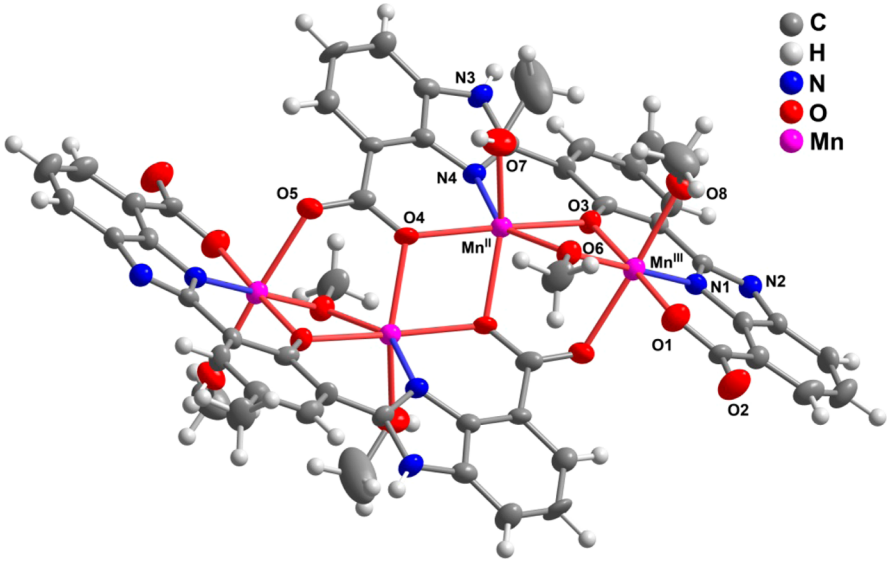

Figure 2. Crystal structure of the tetranuclear Mn complex **2** generated from complex **1**. Reprinted with permission from ref 17. Copyright 2011 Wiley-VCH Verlag GmbH & Co. KGaA.

detailed calculations on the related tetranuclear cluster **4**, in particular because its structure resembles that of the natural Mn_4Ca cluster in the OEC.

In the present study, density functional calculations have been employed to elucidate the mechanism of water oxidation promoted by the bioinspired Mn catalyst **4**. We propose a PSII-like water oxidation mechanism, in which the crucial O−O bond formation takes place in the formal $Mn_4^{IV,IV,IV,V}$ state (known as S_4 in OEC) by direct coupling of a Mn^{IV}-bound terminal oxyl radical and a di-Mn bridged oxo group. This is very similar to a mechanism suggested by model calculations[18−20] for PSII. There is strong spectroscopic evidence that this mechanism is indeed true for PSII.[31−33] All other mechanistic pathways studied, including coupling of the oxyl radical and bridging oxo ligands in other states (corresponding to the S_2 and S_3 states), were found to be associated with higher barriers. These results will undoubtedly help the design of more

dx.doi.org/10.1021/ic5024983 | *Inorg. Chem.* 2015, 54, 342−351

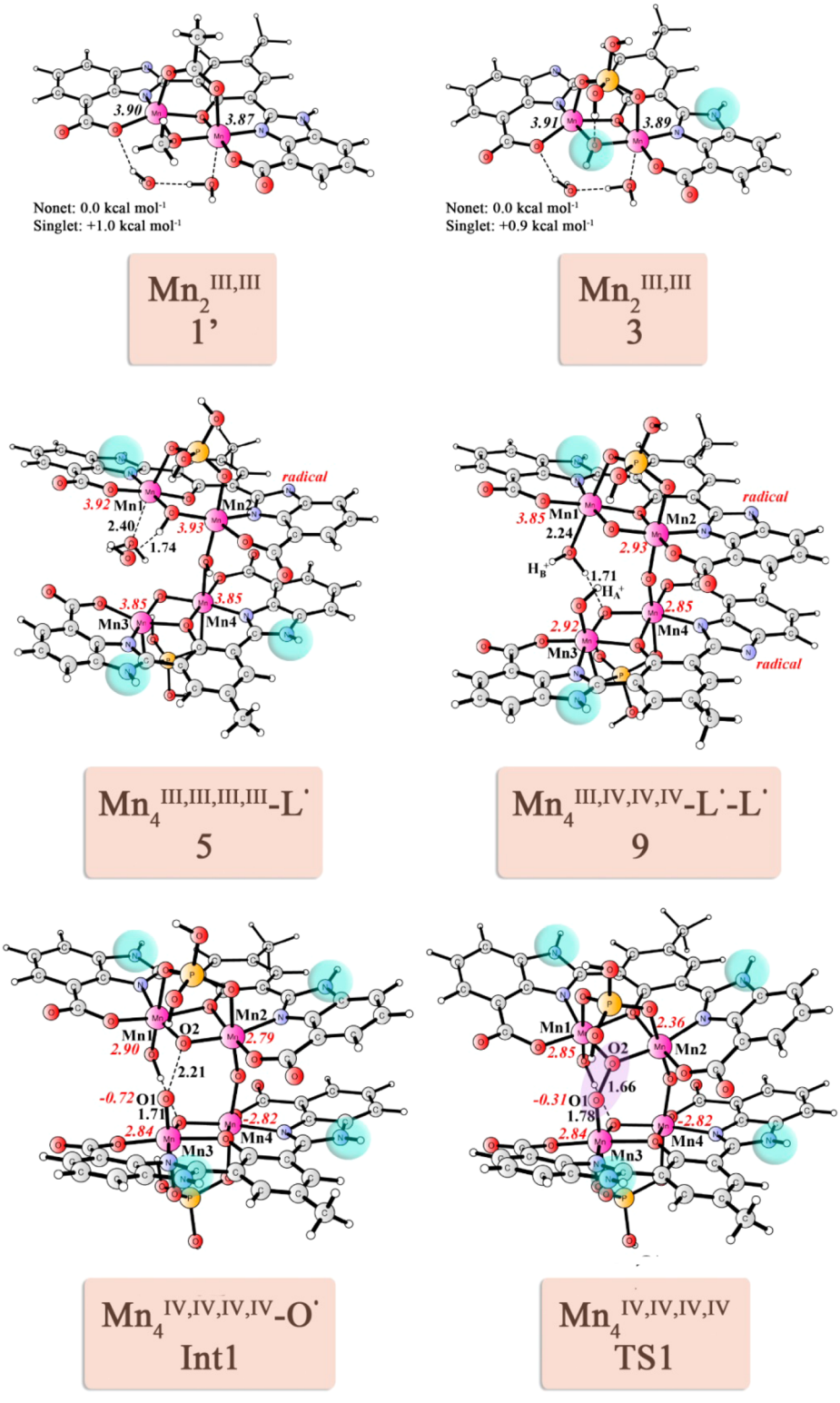

Figure 3. Optimized structures of important intermediates and the transition state for O−O bond formation. For intermediates **1**′ and **3**′, spin densities on Mn for the nonet are shown in italic font and relative energies are given in kilocalories per mole. Distances are given in angstroms, and spin densities on Mn and O1 (only for Int1 and TS1) are shown in red italic font. The position of the ligand radical is also indicated.

efficient and stable Mn-based water-oxidizing complexes (WOCs) in the future.

2. RESULTS AND DISCUSSION

2.1. Formation of the Mn_4 Cluster. On dissolution of complex **1** in phosphate buffer in the presence of air, the methoxide, methanol, and acetate ligands are probably replaced by hydroxide, water, and phosphate to give the $Mn_2^{III,III}$ complex **3**. This is supported by the fact that no electron paramagnetic resonance (EPR) signal can be seen at 77 K.[17] Additional support for the formation of a tetranuclear Mn species was obtained from high-resolution mass spectrometry.

dx.doi.org/10.1021/ic5024983 | Inorg. Chem. 2015, 54, 342−351

Dissolving Mn complex **1** in an aqueous solution, in the presence of 3 equiv of K_3PO_4 (conditions similar to those used in the catalytic experiments), under an air atmosphere resulted in the generation of the tetranuclear Mn complex **5′** (see the Supporting Information, Figure S1), which clearly shows phosphate binding to the metal and displacement of the bridging methoxide by hydroxide.

Our investigation therefore starts with conversion of the $Mn_2^{III,III}$ form of **1** (labeled as **1′** (with two water ligands rather than two methanol ligands); see Figure 3) to complex **3** (Figure 3). The calculations show that this conversion is slightly endergonic by 4.0 kcal mol^{-1}. However, because the concentrations of water and phosphate are considerably greater than that of the catalyst (on the order of millimolar), the equilibrium should be driven toward the formation of complex **3**. As suggested by NMR data[17] and the mass spectrometry measurements, complex **3** can be partly dimerized to form a tetranuclear $Mn_4^{III,III,III,III}$ complex, which is labeled as **4** (Figures S4 and S5, Supporting Information). In **4**, both Mn1 and Mn2 centers are pentacoordinated, and the two water molecules dissociate from the metal centers and form hydrogen bonds with the two bridging hydroxides.

2.2. Redox Intermediates of the Catalytic Cycle. To set up the energy diagram for the whole catalytic cycle, the experimental total driving force was used to fit the proton-coupled electron transfer (PCET)[34,35] redox potentials. This strategy has already been successfully applied in the study of water oxidation of both PSII[18−21] and synthetic catalysts.[36−39] The experimental redox potential of the electrolytic water oxidation at pH 7.2 is 0.804 V vs the standard hydrogen electrode (SHE) and 1.26 V for the $[Ru(bpy)_3]^{3+}$ oxidant. The whole water oxidation process involves four PCET oxidation steps, and therefore, the total driving force is −42.1 kcal mol^{-1} $\{4(0.804 - 1.26) \times 23.06\}$. This experimental value is used to obtain the thermodynamics of each of the four PCET steps.

To start the catalytic cycle, structure **4** (the $Mn_4^{III,III,III,III}$ complex) is oxidized via PCET to the formal $Mn_4^{III,III,III,IV}$ complex **5** (Figure 3), which is similar to the S_0 state in the Kok cycle. A spin population analysis suggests that all four Mn ions are high-spin Mn^{III} ($3d^4$) and a ligand radical is formed lying close to the Mn2 center. The generated ligand radical is delocalized over the phenolate and the deprotonated benzimidazole. The reason for the generation of a ligand radical is that both the phenol oxygen and the imidazole nitrogen adjacent to Mn2 are deprotonated (see further below), which makes this ligand electron-rich and thus redox-active. The electronic structure of **5** can best be described as $Mn_4^{III,III,III,III}$−$L^{\bullet}$, in which $L^{\bullet}$ denotes a ligand radical. This is different from the OEC, where no ligand radical is formed and a "true" Mn^{IV} center is present at S_0. The redox potential of the $Mn_4^{III,III,III,IV}/Mn_4^{III,III,III,III}$ (**5**/**4**) transition was calculated to be 1.17 V, which is 0.09 V lower than the redox potential of the $[Ru(bpy)_3]^{3+}/[Ru(bpy)_3]^{2+}$ oxidant (1.26 V), suggesting an exergonic process for the formation of species **5**. One should be aware that a large number of tautomers, where the protons are located at different positions, need to be calculated to find the tautomer with the lowest energy. For example, 22 tautomers were considered for **5**, and the detailed structures are given in the Supporting Information (Figures S6−S10). Until otherwise specified, only the tautomer with the lowest energy will be discussed in the text below. If all imidazole nitrogen atoms were protonated in the $Mn_4^{III,III,III,IV}/Mn_4^{III,III,III,III}$ (**5**/**4**) transition, the electron would be removed from a Mn center rather than from the ligand. However, this process is less favorable, corresponding to a redox potential of 1.26 V. The imidazole ligand can thus store a redox equivalent and also lower the redox potential of the complex by avoiding the oxidation of the metal center.

The oxidative transition from complex **5** to complex **9**, which initiates O−O bond formation, proceeds through four PCET steps. This is slightly different from the OEC, in which the S_1 to S_2 transition has been suggested to be just a one-electron oxidation while the other transitions are all PCET oxidations.[20] In the conversion of **5** to **6** (Figures S11−S18, Supporting Information), Mn4 is oxidized from Mn^{III} to Mn^{IV} and a proton is released from the hydroxide that bridges Mn2 and Mn4. The redox potential for this transition was calculated to be 1.27 V, almost the same as the redox potential of the oxidant (1.26 V). However, further intramolecular proton transfer from the Mn1-bound imidazole to the Mn2-bound imidazole is exergonic by 2.0 kcal mol^{-1}. This proton transfer process is believed to be very fast in solution and lowers the redox potential to 1.18 V. In complex **6** (analogous to the S_1 state in the OEC), the ligand radical is preserved, and the oxidation state can be interpreted as $Mn_4^{III,III,III,IV}$−$L^{\bullet}$. The corresponding $Mn_4^{III,III,IV,IV}$ state (no ligand radical), where one imidazole nitrogen has been protonated by proton transfer from the Mn1-bound water molecule, is higher in energy by 5.3 kcal mol^{-1}.

Next, a PCET oxidation leads to the formation of species **7** (analogous to the S_2 state in the OEC; see Figures S19−S26, Supporting Information). During this transition, the Mn3 center is oxidized to Mn^{IV} and a proton is released from the Mn3-bound water molecule. The corresponding redox potential for this process was calculated to be 1.41 V. However, intramolecular proton transfer from the Mn1−Mn2 bridging hydroxide to the Mn1-bound imidazole is exergonic by 3.5 kcal mol^{-1}, which lowers the redox potential to 1.25 V. Since all imidazole nitrogen atoms are protonated, the formation of a ligand radical is not favored and thus not formed, and the oxidation state of **7** can be described as $Mn_4^{III,IV,IV,IV}$.

The subsequent step is the transition of complex **7** to complex **8** (analogous to the S_3 state in the OEC; see Figures S27−S30, Supporting Information), which is associated with a redox potential of 1.16 V. In this transition, one electron is removed from a ligand and one proton from the Mn2-bound imidazole. The oxidation state of complex **8** can be described as $Mn_4^{III,IV,IV,IV}$−$L^{\bullet}$. The generation of the $Mn_4^{IV,IV,IV,IV}$ state by transferring a proton from the Mn1-bound water molecule to the imidazole nitrogen is endergonic by 6.1 kcal mol^{-1}. The redox-active character of the designed ligand strongly alleviates the oxidation process, making the oxidation exergonic rather than endergonic.

The final transition from intermediate **8** to intermediate **9** (analogous to the S_4 state in the OEC; see Figure 3 and Figures S31−S34, Supporting Information) is endergonic by 5.3 kcal mol^{-1}, which corresponds to a redox potential of 1.49 V. During the oxidation, an electron is removed from the ligand close to Mn4 coupled with the release of a proton from the imidazole. This leads to the formation of a second ligand radical, and the oxidation state of **9** can thus be described as $Mn_4^{III,IV,IV,IV}$−$L^{\bullet}$−$L^{\bullet}$. Under the catalytic conditions, **8** will be the resting state for O−O bond formation. This is similar to the OEC, in which an oxyl radical is developed during the formation of S_4, with an associated redox potential calculated to be 1.63 V without a membrane gradient.[20] However, no oxyl radical is formed in **9** in the present case, and further

dx.doi.org/10.1021/ic5024983 | Inorg. Chem. 2015, 54, 342−351

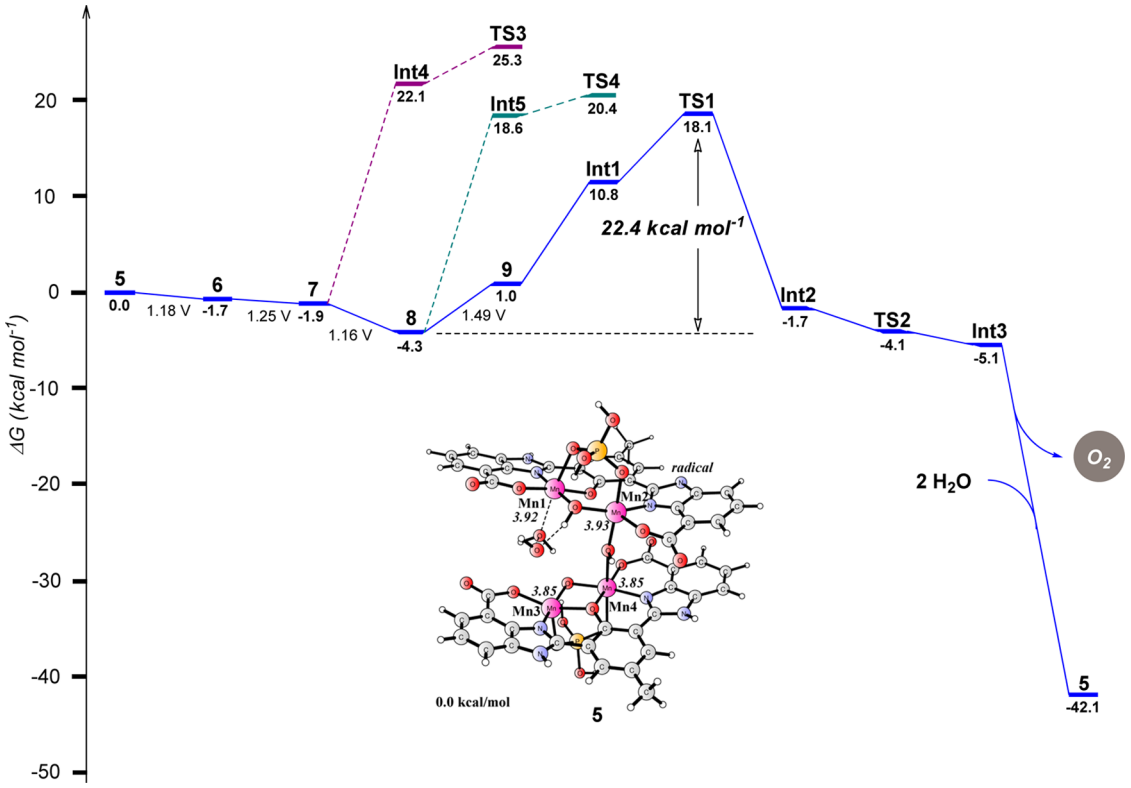

Figure 4. Energy profile for O_2 formation catalyzed by the Mn_4 complex.

intramolecular redox processes must take place to generate an oxyl radical for the subsequent formation of O_2. It should also be pointed out that the redox potentials for the four oxidations (from complex **4** to complex **8**) lie in the range of 1.10−1.30 V, which is close to the onset potential where O_2 evolution starts. This makes it difficult to assign the redox potential peaks in the cyclic and differential pulse voltammetry experiments.

2.3. O−O Bond Formation. From species **9**, an oxyl radical can be created by transferring a proton (H_A^+) from the Mn3-bound hydroxide to an imidazole nitrogen atom. Calculations show that an additional transfer of a proton (H_B^+) from the Mn1-bound water molecule to a second imidazole nitrogen atom results in a less endergonic process (from 11.7 to 9.8 kcal mol^{-1}), labeled as Int1 (Figure 3). When going from complex **9** to Int1, the electronic structure of the complex changes from $Mn_4^{III,IV,IV,IV}$−L•−L• to $Mn_4^{IV,IV,IV,IV}$−O•. For Int1, nine different spin-coupled states were calculated (Table S1, Supporting Information) and the most stable state is a sextet. In this state, the electron of the oxyl radical has an unpaired β electron (1 β), the same as the three unpaired β electrons (3 β) at Mn4, while each of Mn1, Mn2, and Mn3 has three unpaired α electrons (3 α). The oxyl radical (spin density of −0.72) is thus antiferromagnetically coupled with Mn3 (spin density of 2.84), and this spin coupling pattern has also been suggested for other Mn−O complexes.[28,40−42] A Mn^{IV}−oxyl radical is equivalent to the quintet state of Mn^{V}=O. In addition, any attempt to optimize a triplet Mn^{V}−oxo (2 α on Mn) leads to a more stable Mn^{IV}−oxyl state (3 α on Mn and 1 β on O), and spin delocalization on the oxygen moiety is preferred. The energy of this intermediate is 9.8 kcal mol^{-1} higher than that of **9**, which shows that generation of the oxyl radical state from **8** is endergonic by 15.1 kcal mol^{-1} and corresponds to a redox potential of 1.91 V for the direct transition from **8** to Int1, which is about 0.3 V (7 kcal mol^{-1}) higher than that for the OEC.

There are seven other states where the oxyl radical (1 β) interacts antiferromagnetically with Mn3 (3 α), while the spin of all the other three Mn ions can be either parallel (3 α) or antiparallel (3 β) to the three α electrons at Mn3. These states are all of higher energy but within 4 kcal mol^{-1}. There is also a 14-tet state, in which all four Mn^{IV} ions have three α electrons and the oxyl radical (1 α) interacts ferromagenetically with Mn3. The 14-tet state was calculated to be 19.1 kcal mol^{-1} higher than **9**.

From Int1, the O−O bond can be formed between the oxyl radical (O1) and the Mn1−Mn2 bridging oxo moiety, which is similar to the proposed reaction in the OEC.[19,20] In Int1, the relative positions of the two oxygen atoms are held by the bridging oxo group and the hydrogen bond between the Mn1-bound hydroxide and the Mn3−Mn4 bridging oxo group. Due to these two important factors, the structure of the complex is well-organized for O−O bond formation with a distance between O1 and O2 of 2.21 Å. The optimized transition state (TS1) is shown in Figure 3, and the corresponding intrinsic reaction coordinate (IRC)[43] profile is displayed in Figure S37 (Supporting Information). The sextet (333n3n1; see Table S1 for details) was calculated to be the most favorable state with an associated O−O bond formation barrier of only 7.3 kcal mol^{-1} relative to Int1 and 17.1 kcal mol^{-1} relative to **9**. This translates into a total barrier from intermediate **8** of 22.4 kcal mol^{-1} (Figure 4). The experimental turnover frequency has been measured to be 0.027 s^{-1},[17] which can be converted into a barrier of about 20 kcal mol^{-1} and shows that the calculated barrier is in good agreement with the experimental one. At TS1 (sextet, 333n3n1), the nascent O−O bond distance is 1.66 Å, and the Mn3−O1 bond is elongated from 1.71 Å in Int1 to 1.78

dx.doi.org/10.1021/ic5024983 | Inorg. Chem. 2015, 54, 342−351

Table 1. Calculated Redox Potentials (V vs SHE) of Various Redox Couples for the Artificial Mn_4 Complex[a]

artificial Mn_4 complex		OEC	
redox state	calcd redox potential	redox state	calcd redox potential[b]
5 ($Mn_4^{III,III,III,III}$–$L^{\bullet}$)/**4** ($Mn_4^{III,III,III,III}$)	1.17		
6 ($Mn_4^{III,III,III,IV}$–$L^{\bullet}$)/**5** ($Mn_4^{III,III,III,III}$–$L^{\bullet}$)	1.18	S_1/S_0	0.64 (0.67)
7 ($Mn_4^{III,IV,IV,IV}$)/**6** ($Mn_4^{III,III,III,IV}$–$L^{\bullet}$)	1.25	S_2/S_1	0.86 (1.15)
8 ($Mn_4^{III,IV,IV,IV}$–$L^{\bullet}$)/**7** ($Mn_4^{III,IV,IV,IV}$)	1.16	S_3/S_2	1.00 (1.15)
9 ($Mn_4^{III,IV,IV,IV}$–$L^{\bullet}$–$L^{\bullet}$)/**8** ($Mn_4^{III,IV,IV,IV}$–$L^{\bullet}$)	1.49 (1.91)[c]	S_4/S_3	1.63 (1.68)

[a]As a comparison the previously reported redox potentials for the OEC are also shown. [b]For the OEC, data in parentheses are calculated with a membrane gradient (3 pH units). [c]The redox potential for the generation of an oxyl radical is shown in parentheses.

Å in TS1. The O–O bond is formed by combining the β electron from O1 and an α electron from O2. In addition, a β electron from O2 is transferred to Mn2. This can be seen from the spin density on Mn2, which changes from 2.79 at Int1 to 2.36 at TS1. Since Mn2 has three α electrons, this electron transfer leads to Mn2 in an excited state (intermediate-spin rather than high-spin Mn^{III}) in the product. Therefore, a spin crossing is needed after the formation of the product. This situation is different from the one in the OEC where no spin crossing is required. If the d-electrons on Mn2 would have had the same spin direction as the oxyl radical, the electron transfer to Mn2 would have resulted in the ground-state product, in which Mn2 (Mn^{III}) is high-spin rather than intermediate-spin. However, the lowest barrier (sextet, 3n333n1) was surprisingly found to be 4.3 kcal mol^{-1} higher in that case. At the transition state, the O–O bond distance is 1.79 Å, slightly longer than the one mentioned above.

In the resulting intermediate Int2 (Figure S38, Supporting Information), a peroxo is formed, which bridges Mn1, Mn2, and Mn3. The energy of Int2 is 2.7 kcal mol^{-1} lower than that of **9**, and its oxidation state can be described as $Mn_4^{III,IV,IV,IV}$. From Int2, there is a dissociation of the peroxo group from Mn3 via TS2 (Figure S38), coupled with a one-electron transfer from the peroxo unit to Mn3. This step was calculated to be barrierless, with the resulting intermediate Int3 (Figure S38), 6.1 kcal mol^{-1} lower in energy than **9**. At the Int3 state, a superoxide radical is formed, and the oxidation state can be described as $Mn_4^{III,III,IV,IV}$–$O_2^{\bullet-}$. From Int3, O_2 can be released, and two water molecules bind to the Mn centers, thus regenerating complex **5**.

We have also investigated a large number of other possible transition states for the O–O bond formation, but the barriers were all found to be higher than the one discussed above. If a ligand radical is maintained by transferring a proton from the imidazole to the Mn3–Mn4 bridged oxo group, four possibilities can be envisioned (Figure S39, Supporting Information), and the species with the lowest barrier ($TS1_B$) was calculated to be 17.4 kcal mol^{-1}, slightly higher than that for TS1. An alternative scenario is to eliminate a water molecule from **9** to generate an oxo group that bridges Mn1 and Mn3 (**10**, Figure S40, Supporting Information). The oxidation state of **10** can be seen as $Mn_4^{IV,IV,IV,IV}$–$L^{\bullet}$, and a direct coupling of the two bridging oxo groups appears as a viable possibility. However, the barrier was found to be as high as about 40 kcal mol^{-1}, ruling out this possibility. One possible reason is that one bridging oxo must dissociate from one Mn to generate an oxyl radical for the following O–O bond formation step to occur, and this process is quite energy demanding. The mechanistic scenario (direct coupling of two bridging oxo groups) is reminiscent of the O–O bond formation mechanism in the artificial Mn_4 catalyst reported by Dismukes and co-workers.[14,44] A barrier of about 30 kcal mol^{-1} was found in that case,[38] and indeed, light is needed to provide the extra energy to overcome the high barrier.[14]

2.4. Catalyst Degradation. The relatively low TON of catalyst **3** suggests that fast deactivation occurs. The decomposition of Mn complexes may lead to MnO_x nanoparticles that promote water oxidation, as found for a number of cases.[46] However, for the present catalyst, it has been demonstrated to be a true homogeneous catalyst,[17] with no activity observed after catalyst decomposition. However, a possible degradation pathway could be water attack on a ligand radical, which we have recently studied in iron-catalyzed water oxidation.[38] Here, we considered attack of water at the carbon center attached to the phenolate oxygen, which should be the most active site. The optimized reactant complex (**9** + OH_2), transition state, and product are shown in Figure S41 (Supporting Information). The barrier for the water attack was calculated to be 18.7 kcal mol^{-1} relative to the reactant complex, and the reaction is exergonic by 3.8 kcal mol^{-1}. The barrier is thus only 1.6 kcal mol^{-1} higher than that of the O–O bond formation pathway occurring from intermediate **9**. The small barrier difference could explain why a limited TON is achieved for the artificial Mn catalyst. To increase the TON of the catalyst, future ligands have to be designed to avoid water attack on the ligand scaffolds and related side reactions that lead to catalyst deactivation. Interestingly, a tetranuclear Mn water oxidation catalyst has very recently been synthesized using inorganic tungstosilicate as a ligand,[45] in which the ligand modification by water attack or oxidation can be avoided.

2.5. O–O Bond Formation from Intermediates 7 and 8. Oxidation states of the Mn_4Ca cluster in PSII, which differ from the one normally assumed, have also been suggested, in which S_4 has been assigned as $Mn_4^{III,IV,IV,IV}$.[47,48] This oxidation state is actually the same as for intermediate **7** in the present study. To compare the relative reactivities of **7**, **8**, and **9** that have different oxidation states, the barriers for direct O–O bond formation from **7** and **8** were also calculated. For species **7**, which is in the $Mn_4^{III,IV,IV,IV}$ redox state, the generation of an oxyl radical ($Mn_4^{III,III,IV,IV}$–$O^{\bullet}$; Figure S42, Supporting Information) is endergonic by 24.0 kcal mol^{-1}, and the following O–O bond formation step has a barrier of 27.2 kcal mol^{-1} relative to **7**, which is 4.8 kcal mol^{-1} higher than that from **9** ($Mn_4^{III,IV,IV,IV}$–$L^{\bullet}$–$L^{\bullet}$). Similarly, the generation of an oxyl radical from **8** ($Mn_4^{III,IV,IV,IV}$–$O^{\bullet}$; Figure S43, Supporting Information) is endergonic by 22.9 kcal mol^{-1}, and the barrier for O–O bond formation was found to be 24.7 kcal mol^{-1}, which is 2.3 kcal mol^{-1} higher than that from **9**. These results suggest that O–O bond formation in the artificial Mn complex takes place preferentially from **9**, which has the same oxidation state as the generally accepted S_4 state in the OEC.[18−27]

dx.doi.org/10.1021/ic5024983 | Inorg. Chem. 2015, 54, 342−351

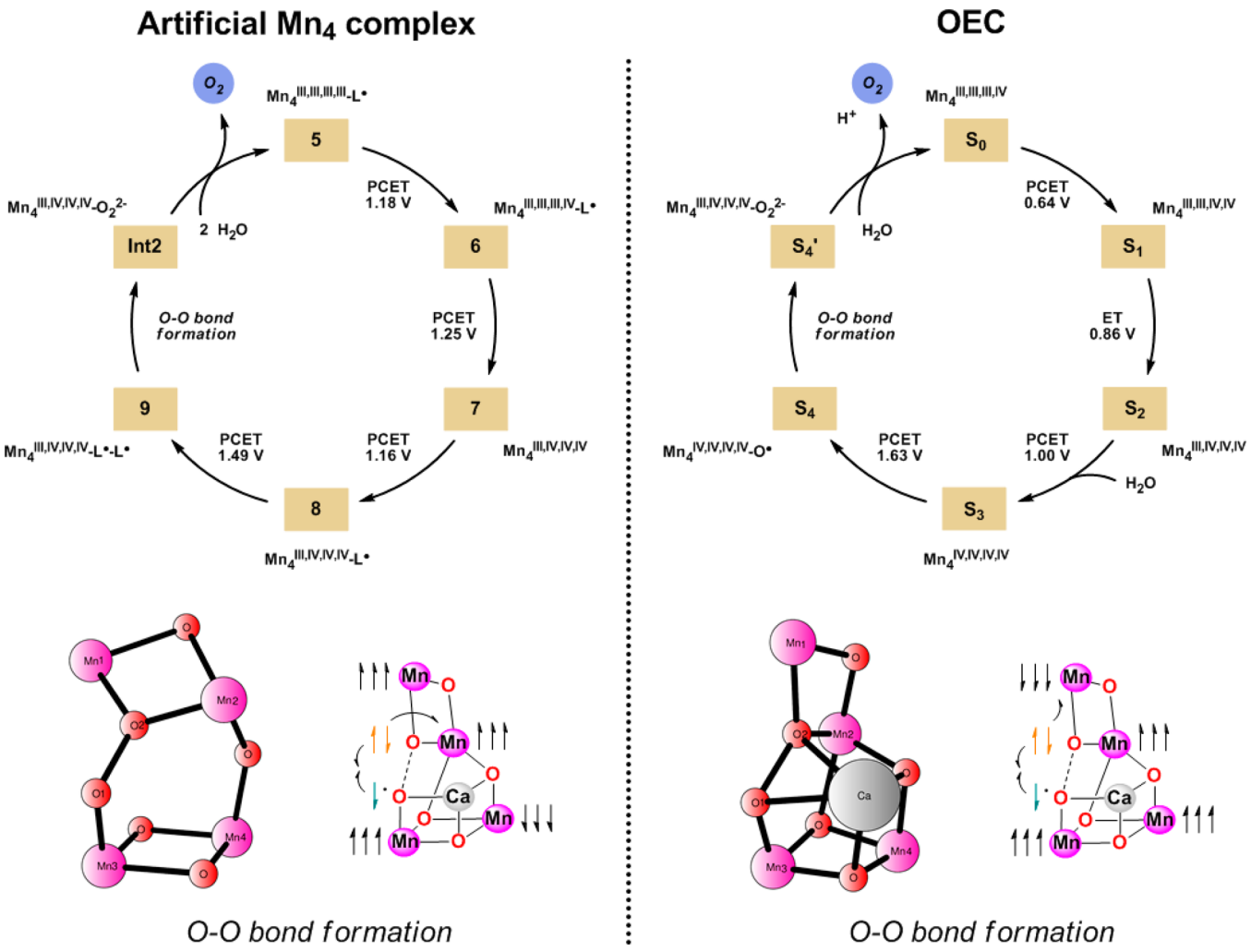

Figure 5. Comparison of the catalytic cycles, transition-state structures, and schematic mechanisms for O−O bond formation in the artificial Mn_4 complex and the OEC.

2.6. Comparison of the OEC in PSII with the Bioinspired Mn Complex. Our calculations show that the studied Mn_4 catalyst has great structural and mechanistic similarities to the OEC. To the best of our knowledge, this is the first synthetic metal complex based on Mn that follows the leading mechanistic suggestion for the O−O bond formation in the OEC. By comparing the electronic structures and energies of various intermediates of the Mn_4 complex and the OEC, we can find the following similarities and differences.

Both systems require the cooperation of four Mn ions to efficiently catalyze the oxidation of water. The O_2 evolution from complex **4** starts with **5** with the formal oxidation state $Mn_4^{III,III,III,IV}$, corresponding to the S_0 state in the catalytic Kok cycle and ends with **9** with the formal $Mn_4^{IV,IV,IV,V}$ state, corresponding to the S_4 state. The transition from **5** to **8** (S_0 to S_3) is exergonic, while the transition from **8** to **9** is endergonic, and intermediate **8** is the resting state in the catalytic cycle. For the synthetic Mn_4 complex, the ligand framework is redox-active, which can facilitate PCET processes and significantly lower the redox potentials for the various transitions. As shown in Table 1, the redox potentials for the synthetic Mn_4 complex are higher than those for the OEC, except for the **8** to **9** (S_3 to S_4) transition, for which the potentials are about the same for the synthetic Mn_4 complex and the OEC. However, the generation of an oxyl radical requires a significant amount of energy which is much higher for the synthetic Mn_4 complex (15.1 kcal mol^{-1}) than for the OEC (3.6 kcal mol^{-1}). The structure of the S_4 state in the OEC consists of six bridging oxo ligands, while there are only three in the synthetic Mn_4 complex in addition to two phenolate ions. The involvement of a multinuclear Mn−oxo core has been suggested to be important for the design of a successful Mn water oxidation catalyst.[49,50] In the Mn_4 complex, the Mn1 and Mn2 centers are bridged by an oxo and a phenolate and the Mn3 and Mn4 centers have the same bridging coordination pattern, while Mn4 and Mn2 are bridged by only one oxo group. In the OEC, Mn2 and Mn3 are bridged also by an oxo group, which is absent in the synthetic Mn core. The critical O−O bond formation step in both the synthetic Mn complex and the OEC proceeds via a direct coupling of an oxyl radical and a di-Mn bridging oxo group (see Figure 5), and during the O−O bond formation, one electron is transferred from the bridging oxo group to the Mn center. However, for the synthetic Mn_4 complex this transfer leads to an excited-state product (intermediate-spin Mn^{III}) rather than to a ground-state product (high-spin Mn^{III}) as in the OEC. A spin crossing is therefore needed in the former case. A plausible reason for this difference is that, in the synthetic Mn_4 complex, after the reduction of Mn2, the ligands on the Jahn−Teller axis are the bridging phenolate and the terminal carboxylate. In addition, O2 maintains a strong interaction with Mn2. By

dx.doi.org/10.1021/ic5024983 | Inorg. Chem. 2015, 54, 342−351

contrast, O2 (Figure 5) is situated on the Jahn−Teller axis in the OEC and dissociates from Mn1 after O−O bond formation. In both cases, the barrier is low (less than 8 kcal mol^{-1}) starting from the oxyl radical state. However, the total barrier for the synthetic Mn_4 complex **4** is still about 10 kcal mol^{-1} higher than that for the OEC due to the greater energy penalty for the formation of the oxyl radical state.

O_2 release starts from the peroxide intermediate by breaking the bond between Mn3 and O1, coupled with a one-electron transfer from the peroxide to Mn3 (Figure 4) and the generation of a superoxide radical as a bridging ligand to Mn1 and Mn2. This process is exergonic and is different from the endergonic step in the OEC.[20,51] Compared to the OEC, the redox potential for the Mn^{IV}/Mn^{III} couple is higher in the synthetic Mn_4 complex, and thus, the reduction of Mn3 by electron transfer from the peroxide is facilitated. In the OEC, direct cleavage of either Mn3−O1 or Mn2−O2 would result in the formation of a terminal superoxide radical bound to one Mn center, which seems to be energetically less favorable. Indeed, recent calculations show that the dissociation of O1 from Mn3 is coupled with binding of O2 to Mn3.[42] In the catalytic cycle of complex **5**, O_2 release is coupled to the binding of two water molecules to regenerate **5**. This is different from the OEC, in which only one water molecule binds to regenerate S_0 while the second water molecule enters the catalytic cycle during the $S_2 \rightarrow S_3$ transition.[20]

3. CONCLUSION

In summary, the water oxidation mechanism has been investigated for a synthetic, bioinspired Mn complex. Both monomeric (dinuclear Mn_2 complex) and dimeric (tetranuclear Mn_4 complex) forms have been considered as potential catalytic entities, which experimentally have been shown to exist in equilibrium in solution. Other intermediates cannot be excluded, such as a dimer, a different tetramer, or even manganese oxide. However, a dimer seems unlikely according to the calculations. Manganese oxide is also unlikely because manganese acetate and similar simple precursors fail to catalyze water oxidation. Also other tetramers are in principle possible, but the chosen one appears most likely because it is actually formed on crystallization. An OEC-like mechanism is proposed, involving the cooperation of four Mn centers. The catalytic cycle is similar to the redox transitions in the OEC, going from a formal $Mn_4^{III,III,III,IV}$ complex to a formal $Mn_4^{IV,IV,IV,V}$ species. The catalysis starts from complex **5**, in which a ligand radical is present and all four Mn centers are in the Mn^{III} state. Four sequential PCET oxidations result in the formation of **9**, with **8** as the resting state. From **9**, intramolecular proton transfer leads to the generation of a Mn^{IV}-bound oxyl radical, which then generates the O−O bond with the Mn1−Mn2 bridged oxo group. This mechanism is very similar to the leading suggestion for the OEC[20] but different from the nucleophilic water attack mechanism on a mononuclear[12] or a dinuclear[28] Mn complex and also the radical coupling mechanism observed for Ru-based catalysts.[52] The total barrier was calculated to be 22.4 kcal mol^{-1} and is in good agreement with the experimental results (20 kcal mol^{-1}). During the O−O bond formation, one β electron from the bridging oxo group is transferred to Mn2 (3 α), leading to a product in the excited state. If the spin of the transferred electron is parallel to those of Mn2, like the OEC, the barrier is about 4 kcal mol^{-1} higher, even though the resulting product is in the ground state. O−O bond formation by coupling two bridging oxo groups was found to have a significantly higher barrier, suggesting that further dehydration to bridge Mn1 and Mn3 leads to an inactive form. Since a ligand radical is present in **9**, the calculations suggested that a water molecule could attack the ligand, leading to catalyst deactivation, similarly to that found in our previous study on iron-catalyzed water oxidation.[38] One may also suspect that the metal could be extracted from the ligand by phosphate, which binds fairly strongly to Mn ions and leads to deactivation. O−O bond formation at the lower oxidation states, starting from **7** or **8**, was also investigated, but the barriers were found to be higher than the one from **9**.

Our present results suggest the following physical design principles for future water oxidation catalyst mimics of the OEC: (1) A Mn-bound terminal water molecule should be present to generate the essential $Mn^{IV}-O^{\bullet}$. If all Mn ions are saturated by organic ligands and bridging oxygen species (oxo or hydroxide), an extra energetic penalty needs to be overcome to generate the oxyl radical. (2) A nucleophilic water attack on the $Mn^{IV}-O^{\bullet}$ seems to be less favorable than a mechanism involving coupling between a bridging oxo and the $Mn^{IV}-O^{\bullet}$, in which no proton transfer occurs in the O−O bond formation step. Therefore, a minimum of three Mn ions are needed to allow an OEC-like O−O bond formation mechanism. (3) A redox-active ligand is helpful to lower the redox potentials for each oxidation step and alleviates the metal centers from being heavily oxidized.

4. COMPUTATIONAL DETAILS

The quantum chemical calculations were made using density functional theory (DFT) with the hybrid B3LYP[53] functional, as implemented in the Gaussian09 program package.[54] For geometry optimizations, the SDD[55] pseudopotential was used for Mn and 6-31G(d,p) for the P, C, N, O, and H elements (labeled as BSI). On the basis of these optimized geometries, more accurate energies were obtained by performing single-point calculations using the B3LYP* functional (15% exact exchange)[56] and a larger basis set, where all elements, except Mn, were described by 6-311+G(2df,2p) (labeled as BSII). Very recent comparison of the performance of different functionals on the energetics of water oxidation by OEC suggested that B3LYP* gave the most reliable results.[57] The water solvation effects were taken into account by employing the SMD[58] continuum solvation model at the B3LYP*/BSII level. Analytic frequency calculations were carried out at the same level of theory as the geometry optimization for all structures to characterize their nature as either minima or transition states and also to compute the Gibbs free energy corrections. The reaction pathway for the O−O bond formation was subjected to IRC[43] analysis to trace its path and to confirm that the optimized TS structure connects the reactant and product. For all species except water, the concentration correction of 1.9 kcal mol^{-1} at room temperature was added, which accounts for the change of standard state from 1 atm (24.5 L mol^{-1}, 298.15 K) for the ideal gas to 1 M (1 mol L^{-1}) in solution. For water, the correction is 4.3 kcal mol^{-1} as the standard state of the water solvent is 55.6 M. In addition, for the solvation free energy of water, the experimental value of −6.3 kcal mol^{-1} is used.[59] The final free energies reported are the B3LYP* energies including the Gibbs free energy correction from B3LYP and dispersion correction using the D2 method developed by Grimme.[60]

To calculate the redox potentials of various oxidation steps, the experimental absolute redox potential of the $[Ru(bpy)_3]^{3+}/[Ru(bpy)_3]^{2+}$ couple (1.26 + 4.281 V) was used as a reference,[61] which corresponds to an electron affinity of 127.8 kcal/mol. For PCET oxidations, the experimental driving force ($4(0.804 - 1.26) \times 23.06 = -42.1$ kcal mol^{-1}) was used to derive the reference redox potential, which corresponds to 405.9 kcal mol^{-1} for the release of (H^+, e^-) (for more details on the methodology, see ref 39). For the PCET redox potentials without fitting, the experimental value of −264.0 kcal mol^{-1}

dx.doi.org/10.1021/ic5024983 | Inorg. Chem. 2015, 54, 342−351

for the solvation free energy of a proton is used.[59] Comparisons with/without fitting and the use of different functionals are shown in the Supporting Information (Figures S44–S46).

■ ASSOCIATED CONTENT

Supporting Information

Structures and Cartesian coordinates of Mn_4 and Mn_2 complexes and energy diagrams for different functionals. This material is available free of charge via the Internet at http://pubs.acs.org.

■ AUTHOR INFORMATION

Corresponding Authors

*E-mail: rongzhen@organ.su.se.
*E-mail: ps@organ.su.se.

Notes

The authors declare no competing financial interest.

■ ACKNOWLEDGMENTS

We acknowledge the Swedish Research Council, the Carl Trygger Foundation, and the Knut and Alice Wallenberg Foundation for financial support. Computer time was generously provided by the Swedish National Infrastructure for Computing.

■ REFERENCES

(1) Ferreira, K. N.; Iverson, T. M.; Maghlaoui, K.; Barber, J.; Iwata, S. *Science* **2004**, *303*, 1831–1838.
(2) Loll, B.; Kern, J.; Saenger, W.; Zouni, A.; Biesiadka, J. *Nature* **2005**, *438*, 1040–1044.
(3) Guskov, A.; Kern, J.; Gabdulkhakov, A.; Broser, M.; Zouni, A.; Saenger, W. J. *Nat. Struct. Mol. Biol.* **2009**, *16*, 334–341.
(4) Umena, Y.; Kawakami, K.; Shen, J.-R.; Kamiya, N. *Nature* **2011**, *473*, 55–60.
(5) Kok, B.; Forbush, B.; McGloin, M. *Photochem. Photobiol.* **1970**, *11*, 457–475.
(6) Yachandra, V. K.; DeRose, V. J.; Latimer, M. J.; Mukerji, I.; Sauer, K.; Klein, M. P. *Science* **1993**, *260*, 675–679.
(7) Limburg, J.; Vrettos, J. S.; Liable-Sands, L. M.; Rheingold, A. L.; Crabtree, R. H.; Brudvig, G. W. *Science* **1999**, *283*, 1524–1527.
(8) Shimazaki, Y.; Nagano, T.; Takesue, H.; Ye, B.-H.; Tani, F.; Naruta, Y. *Angew. Chem., Int. Ed.* **2004**, *43*, 98–100.
(9) Yagi, M.; Narita, K. *J. Am. Chem. Soc.* **2004**, *126*, 8084–8085.
(10) Poulsen, A. K.; Rompel, A.; McKenzie, C. J. *Angew. Chem., Int. Ed.* **2005**, *44*, 6916–6920.
(11) Beckmann, K.; Uchtenhagen, H.; Berggren, G.; Anderlund, M. F.; Thapper, A.; Messinger, J.; Styring, S.; Kurz, P. *Energy Environ. Sci.* **2008**, *1*, 668–676.
(12) Gao, Y.; Åkermark, T.; Liu, J.; Sun, L.; Åkermark, B. *J. Am. Chem. Soc.* **2009**, *131*, 8726–8727.
(13) Young, K. J.; Takase, M. K.; Brudvig, G. W. *Inorg. Chem.* **2013**, *52*, 7615–7622.
(14) Brimblecombe, R.; Koo, A.; Dismukes, G. C.; Swiegers, G. F.; Spiccia, L. *J. Am. Chem. Soc.* **2010**, *132*, 2892–2894.
(15) Kanady, J. S.; Tsui, E. Y.; Day, M. W.; Agapie, T. *Science* **2011**, *333*, 733–736.
(16) Kärkäs, M. D.; Verho, O.; Karlsson, E. A.; Åkermark, B. *Chem. Rev.* **2014**, DOI: 10.1021/cr400572f.
(17) Karlsson, E. A.; Lee, B.-L.; Åkermark, T.; Johnston, E. V.; Kärkäs, M. D.; Sun, J.; Hansson, Ö.; Bäckvall, J.-E.; Åkermark, B. *Angew. Chem., Int. Ed.* **2011**, *50*, 11715–11718.
(18) Siegbahn, P. E. M. *Chem.—Eur. J.* **2006**, *12*, 9217–9227.
(19) Siegbahn, P. E. M. *Acc. Chem. Res.* **2009**, *42*, 1871–1880.
(20) Siegbahn, P. E. M. *Biochim. Biophys. Acta, Bioenerg.* **2013**, *1827*, 1003–1019.
(21) Siegbahn, P. E. M. *J. Am. Chem. Soc.* **2013**, *135*, 9442–9449.
(22) Ames, W.; Pantazis, D. A.; Krewald, V.; Cox, N.; Messinger, J.; Lubitz, W.; Neese, F. *J. Am. Chem. Soc.* **2011**, *133*, 19743–19757.
(23) Pantazis, D. A.; Ames, W.; Cox, N.; Lubitz, W.; Neese, F. *Angew. Chem., Int. Ed.* **2012**, *51*, 9935–9940.
(24) Gatt, P.; Petrie, S.; Stranger, R.; Pace, R. J. *Angew. Chem., Int. Ed.* **2012**, *51*, 12025–12028.
(25) Galstyan, A.; Robertazzi, A.; Knapp, E. W. *J. Am. Chem. Soc.* **2012**, *134*, 7442–7449.
(26) Bovi, D.; Narzi, D.; Guidoni, L. *Angew. Chem., Int. Ed.* **2013**, *52*, 11744–11749.
(27) Kurashige, Y.; Chan, G. K.-L.; Yani, T. *Nat. Chem.* **2013**, *5*, 660–666.
(28) Lundberg, M.; Blomberg, M. R. A.; Siegbahn, P. E. M. *Inorg. Chem.* **2004**, *43*, 264–274.
(29) Privalov, T.; Sun, L.; Åkermark, B.; Liu, J.; Gao, Y.; Wang, M. *Inorg. Chem.* **2007**, *46*, 7075–7086.
(30) Sameera, W. M. C.; McKenzie, C. J.; McGrady, J. E. *Dalton Trans.* **2011**, *40*, 3859–3870.
(31) Rapatskiy, L.; Cox, N.; Savitsky, A.; Ames, W. M.; Sander, J.; Nowaczyk, M. M.; Rögner, M.; Boussac, A.; Neese, F.; Messinger, J.; Lubitz, W. *J. Am. Chem. Soc.* **2012**, *134*, 16619–16634.
(32) Navarro, M. P.; Ames, W. M.; Nilsson, H.; Lohmiller, T.; Pantazis, D. A.; Rapatskiy, L.; Nowaczyk, M. M.; Neese, F.; Boussac, A.; Messinger, J.; Lubitz, W.; Cox, N. *Proc. Natl. Acad. Sci. U.S.A.* **2013**, *110*, 15561–15566.
(33) Cox, N.; Retegan, M.; Neese, F.; Pantazis, D. A.; Boussac, A.; Lubitz, W. *Science* **2014**, *345*, 804–808.
(34) Dempsey, J. L.; Winkler, J. R.; Gray, H. B. *Chem. Rev.* **2010**, *110*, 7024–7039.
(35) Weinberg, D. R.; Gagliardi, C. J.; Hull, J. F.; Murphy, C. F.; Kent, C. A.; Westlake, B. C.; Paul, A.; Ess, D. H.; McCafferty, D. G.; Meyer, T. J. *Chem. Rev.* **2012**, *112*, 4016–4093.
(36) Li, X.; Chen, G.; Schinzel, S.; Siegbahn, P. E. M. *Dalton Trans.* **2011**, *40*, 11296–11307.
(37) Li, X.; Siegbahn, P. E. M. *J. Am. Chem. Soc.* **2013**, *135*, 13804–13813.
(38) Liao, R.-Z.; Li, X.; Siegbahn, P. E. M. *Eur. J. Inorg. Chem.* **2014**, 728–741.
(39) Liao, R.-Z.; Siegbahn, P. E. M. *ACS Catal.* **2014**, *4*, 3937–3949.
(40) Balcells, D.; Moles, P.; Blakemore, J. D.; Raynaud, C.; Brudvig, G. W.; Crabtree, R. H.; Eisenstein, O. *Dalton Trans.* **2009**, 5989–6000.
(41) Busch, M.; Ahlberg, E.; Panas, I. *Phys. Chem. Chem. Phys.* **2011**, *13*, 15069–15076.
(42) Sameera, W. M. C.; McKenzie, C. J.; McGrady, J. E. *Dalton Trans.* **2011**, *40*, 3859–3870.
(43) Gonzalez, C.; Schlegel, H. B. *J. Chem. Phys.* **1989**, *90*, 2154–2161.
(44) Kuznetsov, A. E.; Geletii, Y. V.; Hill, C. L.; Musaev, D. G. *J. Phys. Chem. A* **2010**, *114*, 11417–11424.
(45) Al-Oweini, R.; Sartorel, A.; Bassil, B. S.; Natali, M.; Berardi, S.; Scandola, F.; Kortz, U.; Bonchio, M. *Angew. Chem., Int. Ed.* **2014**, *53*, 11182–11185.
(46) Hocking, R. K.; Malaeb, R.; Gates, W. P.; Patti, A. F.; Chang, S. L. Y.; Devlin, G.; MacFarlane, D. R.; Spiccia, L. *ChemCatChem* **2014**, *6*, 2028–2038.
(47) Carrell, T. G.; Tyryshkin, A. M.; Dismukes, G. C. *J. Biol. Inorg. Chem.* **2002**, *7*, 2–22.
(48) Kuzek, D.; Pace, R. J. *Biochim. Biophys. Acta, Bioenerg.* **2001**, *1503*, 123–137.
(49) Wiechen, M.; Berends, H.-M.; Kurz, P. *Dalton. Trans.* **2012**, *41*, 21–31.
(50) Wiechen, M.; Najafpour, M. M.; Allakhverdiev, S. I.; Spiccia, L. *Energy Environ. Sci.* **2014**, *7*, 2203–2212.
(51) Li, X.; Siegbahn, P. E. M. Submitted for publication..
(52) Nyhlén, J.; Duan, L. L.; Åkermark, B.; Sun, L.; Privalov, T. *Angew. Chem., Int. Ed.* **2010**, *49*, 1773–1777.
(53) Becke, A. D. *J. Chem. Phys.* **1993**, *98*, 5648–5652.
(54) Frisch, M. J.; Trucks, G. W.; Schlegel, H. B.; Scuseria, G. E.; Robb, M. A.; Cheeseman, J. R.; Scalmani, G.; Barone, V.; Mennucci,

B.; Petersson, G. A.; Nakatsuji, H.; Caricato, M.; Li, X.; Hratchian, H. P.; Izmaylov, A. F.; Bloino, J.; Zheng, G.; Sonnenberg, J. L.; Hada, M.; Ehara, M.; Toyota, K.; Fukuda, R.; Hasegawa, J.; Ishida, M.; Nakajima, T.; Honda, Y.; Kitao, O.; Nakai, H.; Vreven, T.; Montgomery, J. A., Jr.; Peralta, J. E.; Ogliaro, F.; Bearpark, M.; Heyd, J. J.; Brothers, E.; Kudin, K. N.; Staroverov, V. N.; Kobayashi, R.; Normand, J.; Raghavachari, K.; Rendell, A.; Burant, J. C.; Iyengar, S. S.; Tomasi, J.; Cossi, M.; Rega, N.; Millam, M. J.; Klene, M.; Knox, J. E.; Cross, J. B.; Bakken, V.; Adamo, C.; Jaramillo, J.; Gomperts, R.; Stratmann, R. E.; Yazyev, O.; Austin, A. J.; Cammi, R.; Pomelli, C.; Ochterski, J. W.; Martin, R. L.; Morokuma, K.; Zakrzewski, V. G.; Voth, G. A.; Salvador, P.; Dannenberg, J. J.; Dapprich, S.; Daniels, A. D.; Farkas, Ö.; Foresman, J. B.; Ortiz, J. V.; Cioslowski, J.; Fox, D. J. *Gaussian 09*, revision C.01; Gaussian, Inc.: Wallingford, CT, 2009.

(55) Dolg, M.; Wedig, U.; Stoll, H.; Preuss, H. *J. Chem. Phys.* **1987**, *86*, 866−872.

(56) Reiher, M.; Salomon, O.; Hess, B. A. *Theor. Chem. Acc.* **2001**, *107*, 48−55.

(57) Siegbahn, P. E. M.; Blomberg, M. R. A. *J. Chem. Theory Comput.* **2014**, *10*, 268−272.

(58) Marenich, A. V.; Cramer, C. J.; Truhlar, D. G. *J. Phys. Chem. B* **2009**, *113*, 6378−6396.

(59) Camaioni, D. M.; Schwerdtfeger, C. A. *J. Phys. Chem. A* **2005**, *109*, 10795−10797.

(60) Grimme, S. *J. Comput. Chem.* **2006**, *27*, 1787−1799.

(61) Isse, A. A.; Gennaro, A. *J. Phys. Chem. B* **2010**, *114*, 7894−7899.